IEEE Photonics Journal
An IEEE Photonics Society Publication

Open Access

Generation of an Ultra-Long Optical Needle Induced by an Azimuthally Polarized Beam

Volume 13, Number 1, February 2021

Liwei Liu
Lifang Shi
Fanxing Li
Siyang Yu
Simo Wang
Jialin Du
Min Liu
Bo Qi
Wei Yan

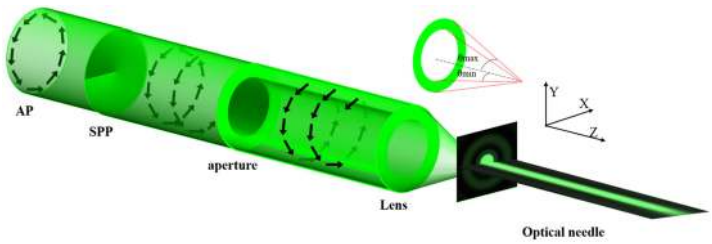

DOI: 10.1109/JPHOT.2020.3047842

Generation of an Ultra-Long Optical Needle Induced by an Azimuthally Polarized Beam

Liwei Liu,[1,2] **Lifang Shi**,[1] **Fanxing Li**,[1] **Siyang Yu**,[1] **Simo Wang**,[1,2] **Jialin Du**,[1,2] **Min Liu**,[1] **Bo Qi**,[1] **and Wei Yan**[1]

[1]Institute of Optics and Electronics, Chinese Academy of Sciences, Chengdu 610209, China
[2]University of Chinese Academy of Sciences, Beijing 100049, China

DOI:10.1109/JPHOT.2020.3047842

Manuscript received November 8, 2020; revised December 19, 2020; accepted December 24, 2020. Date of publication December 29, 2020; date of current version January 11, 2021. This work was supported in part by the National R&D Program of China under Grant 2017YFC0804900, in part by the Instrument Development of Chinese Academy of Sciences under Grants YJKYYQ20180008 and YJKYYQ20180006, in part by the Sichuan Science and Technology Program under Grant 2020JDJQ0007, in part by Youth Innovation Promotion Association, Chinese Academy of Sciences (CAS); CAS "Light of West China" Program, in part by the Microelectronic Equipment Sichuan Province Youth Science and Technology Innovation Team under Grant J17S006, and in part by the Microelectronic Equipment Sichuan Youth Science and Technology Innovation Research Team under Grant 2016TD0021. Corresponding authors: Lifang Shi; Fanxing Li (e-mail: shilifang@ioe.ac.cn, lifanxing15@mails.ucas.ac.cn).

Abstract: In this manuscript, a method of generating an ultra-long optical needle (depth-to-width ratio 37.5:1) is proposed and demonstrated by focusing an azimuthally polarized beam. In theory, the action mechanism between the incident beam and the amplitude modulation element, the spiral phase modulation element, the focusing lens were studied based on the Richards and Wolf's theory. The relationship between the intensity distribution of the optical needle and the structure parameter of the element were obtained, thus leading to the complete design model and design standard. In experiment, the annular amplitude modulation element and spiral phase modulation element were fabricated by lithography. The optical needle was obtained based on a custom-designed optical setup in our laboratory. The optical system consists of an annular aperture (3.9-mm inner diameter, 80-μm annular width), a spiral phase plate (topological charge of 1), and an objective lens with numerical aperture of 0.95. Finally, an optical needle with a subwavelength size (0.416λ) and an ultra-long depth of focus (15.6λ) was obtained, showing an excellent agreement with our theoretical model.

Index Terms: Vector light field, optical needles, azimuthally polarized beam, light field modulation.

1. Introduction

Optical needles with sub-wavelength spot and ultra-long depth-of-focus (DOF) are attractive for various applications, including lithography [1], optical data storage [2] and super-resolution imaging [3]. However, it is difficult to obtain sub-wavelength spot and ultra-long DOF in the focusing system due to the diffraction limit [4]. The vector light field [5]–[10] has attracted extensive attention because its special electric field distribution can break this limitation [11]. Furthermore, the vector

light fields used to generate the optical needle are mainly radially polarized (RP) and azimuthally polarized (AP) beams. In terms of modulation technologies based on RP beams, in 2008, Wang *et al.* [12] proposed to modulate the phase of RP beams by using the binary optical element. An optical needle with a full width at half maximum (FWHM) of 0.43λ and longitudinal full width at half maximum (LFWHM) of 4λ was generated by focusing with an objective lens of NA $= 0.95$. Such a breakthrough promoted the study of super-resolution nano optical needles induced by RP beams. After that, different methods of modulating the RP beam to generate optical needles have been continuously reported [13]–[18]. In these studies, Huang *et al.* [13] showed that adjusting the area outside the normalized radius, R $= 0.5293$ of the light field, is more conducive to extending the DOF. In addition to the phase modulation, this research indicates that increasing the proportion of the large angular component of the incident beam can effectively extend the DOF. Then Zhan *et al.* [18] used a binary optical element, which consists of one zero transmission belt in the central area and four belts with transmissions of -1 and $+1$ alternately in the outer region, to obtain an optical needle with a LFWHM of more than 10λ by simulation. However, the study of optical needles induced by RP beam is mainly at the stage of simulation analysis because of the complexity of the experimental system and the difficulty in characterizing the structure of the optical needle. No relevant experimental verification appeared until recent years [19]–[21]. Compared with RP beams, there are few studies on obtaining optical needles with AP beams [22]–[25]. Therefore, the potential and advantage of AP beams in generating optical needles have not been systematically analyzed and explored [26], [27]. However, similar to RP beam, the AP beam also has perfect rotationally symmetric distribution, symmetric electric field distribution and special polarization distribution [28]–[33], making it possible to generate ultra-long optical needles with a sub-wavelength spot. Furthermore, there is a lack of systematic and theoretical analysis of this technology, whereas the mechanism and theoretical model need to be verified by experiments.

In this paper, we perform a thorough study of the generation of optical needles induced by AP beams, along with a modulation model based on AP beams. In particular, the amplitude modulation element, spiral phase modulation element and the objective lens are used to generate the ultra-long optical needle. The action mechanism between the AP beam and different elements is analyzed to form a complete theoretical design system. We also prove that the AP beam has a significant advantage over the RP beam in generating optical needles by comparing the intensity distributions of focusing spots. Furthermore, the influence of the NA of the objective lens and the amplitude modulator parameters on the spot size and DOF are analyzed. Finally, the modulation elements fabricated by lithography are used for verification experiments. In the experiment, we obtain an optical needle with a subwavelength size (FWHM $= 0.416\lambda$) and an ultra-long DOF (LFWHM $= 15.6\lambda$), proving the feasibility and superiority of using AP beams for optical needle generation.

2. Principle and Model

The modulation model based on the AP beam established in this manuscript is shown in Fig. 1, which is mainly composed of the AP beam, spiral phase plate (SPP), annular aperture and objective lens. The polarization state is presented by the space-variant arrows. In the model, the AP beam with the vortex wavefront (APV beam) is obtained by the phase modulation AP beam with SPP. The reason for this modulation is that the vortex wavefront is conducive to the formation and extension of the electric field component on the optical axis during the focusing process. Furthermore, the APV annular beam is obtained by the amplitude modulation APV beam through an annular aperture. Under the amplitude modulation, the small angular component of the incident light is removed and the large angular component is retained, which are beneficial to the extension of DOF and the compression of spot in the focusing process. Finally, the APV annular beam is focused via the objective lens to generate an optical needle with an ultra-long DOF. As a result, the ultra-long optical needle with sub-wavelength spot is obtain by focusing AP beam by the use of the annular aperture, SPP, and focusing lens in the above process. The principle analysis of the model is as follows.

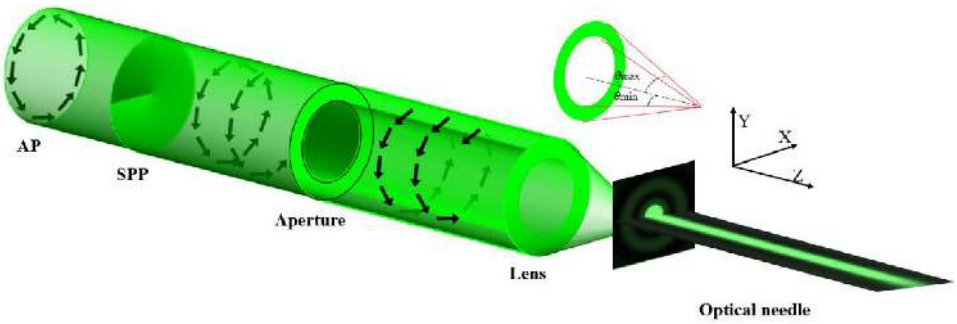

Fig. 1. Sketch of shaping optical needle induced by AP beam.

In the model, the apodization function $l(\theta)$ for the incident AP Laguerre-Gaussian beam is given by Eq. (1):

$$l(\theta) = \frac{\beta^2 \sin\theta}{\sin^2\theta_{\max}} \exp\left[-\beta\left(\frac{\sin\theta}{\sin\theta_{\max}}\right)^2\right] L_1\left[2\left(\frac{\beta\sin\theta}{\sin\theta_{\max}}\right)^2\right], \tag{1}$$

where β is the ratio of the pupil radius to the beam waist, $L_1(x)$ is the first order Laguerre function, and $\theta_{\max}$ is the maximum convergence angle when the beam is focused. Based on the Richard and Wolf's theory [34], [35], when focusing the AP beam with a lens, the electric field in the focusing region can be expressed as:

$$E(r,\varphi,z) = \begin{bmatrix} E_r \\ E_\varphi \\ E_z \end{bmatrix} = \frac{2\pi f}{\lambda} \int_{\theta_{\min}}^{\theta_{\max}} \begin{bmatrix} 0 \\ l(\theta)\sqrt{\cos\theta}\sin\theta J_1(kr\sin\theta)\exp(ikz\cos\theta)\mathrm{d}\theta \\ 0 \end{bmatrix}, \tag{2}$$

where r, φ and z are position coordinates in cylindrical coordinates, f is the focal length of the lens, $\theta_{\min}$ is the minimum convergence angle, and $\theta_{\min} > 0$ indicates that the incident beam is annular; NA is the numerical aperture of the objective lens, $\theta_{\max} = \sin^{-1}(\mathrm{NA}/n)$, n is the refraction index of free space; $J_1(r)$ is the first order Bessel function. Based on Eq. (2), we can analyze the light intensity distribution of the focusing spot of the AP beam. When the upper and lower limits of the integration are determined, the intensity distribution is mainly determined by the $J_1(r)$. However, for the first order Bessel function, the fact that $J_1(0) = 0$ indicates the zero light intensity on the optical axis. In fact, the intensity distribution along the radial direction of the focusing spot is similar to $J_1(r)$, making the focusing spot an optical tunnel. However, when a SPP with the topological charge number m is used to add the vortex phase to the AP beam, Eq. (2) is changed to the following form:

$$\begin{aligned} E(r,\varphi,z) &= \begin{bmatrix} E_r \\ E_\varphi \\ E_z \end{bmatrix} \\ &= \frac{\pi f}{\lambda} \int_{\theta_{\min}}^{\theta_{\max}} \begin{bmatrix} -l(\theta)\sqrt{\cos\theta}\sin\theta\exp(ikz\cos\theta)\exp(im\varphi)\ldots \\ \left[i^{m+1}J_{m+1}(kr\sin\theta) - i^{m-1}J_{m-1}(kr\sin\theta)\right]\mathrm{d}\theta \\ il(\theta)\sqrt{\cos\theta}\sin\theta\exp(ikz\cos\theta)\exp(im\varphi)\ldots \\ \left[i^{m+1}J_{m+1}(kr\sin\theta) + i^{m-1}J_{m-1}(kr\sin\theta)\right]\mathrm{d}\theta \\ 0 \end{bmatrix}, \end{aligned} \tag{3}$$

we also focus on the Bessel functions in Eq. (3). When $m = 1$, the Bessel function terms in Eq. (3) can be approximately expressed as $J_2(r) \pm J_0(r)$. The term $J_0(r)$ has the similar distribution to the Gaussian profile, where the maximum exits at $r = 0$. Therefore, the optical needle can be generated by focusing the APV beam. Furthermore, the ultra-long optical needle can be achieved by modulating the APV beam into an APV annular beam using an annular aperture, which is

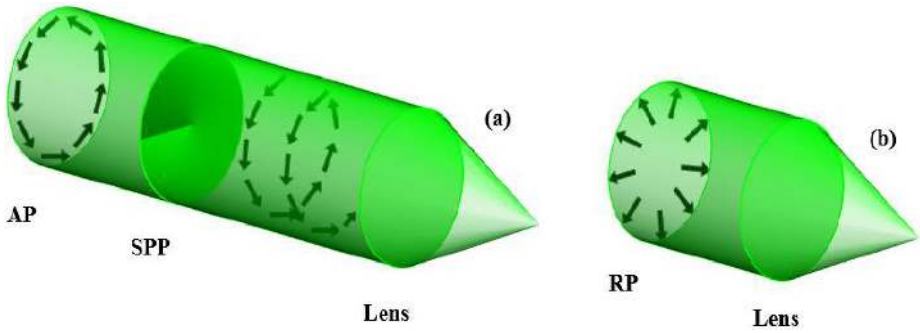

Fig. 2. Models of focusing (a) AP beam and (b) RP beam.

determined by the E_r and E_φ terms in Eq. (3). Note that E_r mainly affects the spot size and E_r mainly affects the DOF. Particularly, with the increase of $\theta_{\min}$, the reduced E_r and increased E_φ lead to the ultra-long optical needle.

The ultra-long optical needle illustrated in Fig. 1 is generated by focusing the APV annular beam. According to Fig. 1 and (1), the upper ($\theta_{\max}$) and lower ($\theta_{\min}$) limits of the integral have the greatest influence on the focusing spot. These two parameters are determined by the NA of the objective lens and the annular width of the beam. Therefore, we will comprehensively analyze the influence of NA and annular width on the focusing spot.

3. Analysis

Firstly, the focusing characteristics of the AP beam are analyzed and compared with the RP beam. Secondly, the influence of the focusing structure parameters on the focusing effect is analyzed, and the relationship between the NA of the focusing lens and the intensity distribution of the focusing spot is obtained. Thirdly, the influence of amplitude modulation element is studied, and the relation between the annular width of the APV beam and the intensity distribution of the focusing field is obtained. Finally, based on the above analysis, the theoretical design model and standard are obtained.

3.1 Comparison of Focusing Spot Between Azimuthally and Radically Polarized Beams

The focusing spot of the APV beam and RP beam is studied. Fig. 2(a) and (b) shows the focusing models of the APV beam and RP beam, respectively. For the AP beam, it is necessary to generate the optical needle by using SPP with m $=$ 1, and the electric field in the focusing region is given in Eq. (3). For the RP beam, the phase modulation is not required, and the electric field can be expressed as:

$$E(r,\varphi,z) = \begin{bmatrix} E_r \\ E_\varphi \\ E_z \end{bmatrix} = \frac{2\pi f}{\lambda} \int_{\theta_{\min}}^{\theta_{\max}} \begin{bmatrix} l(\theta)\sqrt{\cos\theta}\sin\theta\cos\theta J_1(kr\sin\theta)\exp(ikz\cos\theta)\mathrm{d}\theta \\ 0 \\ il(\theta)\sqrt{\cos\theta}\sin^2\theta J_1(kr\sin\theta)\exp(ikz\cos\theta)\mathrm{d}\theta \end{bmatrix}. \quad (4)$$

Eq. (3) and Eq. (4) are used to calculate the light field distribution of the focusing spot under different NAs. The software MATLAB was used to solve the integral in the equation to obtain the intensity distribution of the focused light field. The FWHM and LFWHM of the focusing spot are listed in the Table I. We learn from the table that the size and DOF decrease with the increase of NA. However, for the RP beam, both FWHM and LFWHM are 0 when NA$<$ 0.75. As an illustration, the light intensity distribution along the optical axis at the NA $=$ 0.16, 0.198, 0.247, 0.295, 0.389 and

TABLE 1
FWHM and LFWHM of APV and RP Beams Under Different NAs

NA	FWHM of AP(λ)	FWHM of RP(λ)	LFWHM of AP(λ)	LFWHM of RP(λ)
0.05	10.694	0	768.268	0
0.06	8.914	0	533.566	0
0.07	7.642	0	392.046	0
0.08	6.688	0	300.194	0
0.09	5.946	0	237.222	0
0.1	5.344	0	192.178	0
0.13	4.122	0	113.776	0
0.16	3.352	0	75.16	0
0.198	2.688	0	48.156	0
0.247	2.158	0	30.874	0
0.295	1.804	0	21.486	0
0.389	1.368	0	12.152	0
0.478	1.108	0	7.834	0
0.565	0.938	0	5.488	0
0.644	0.82	0	4.076	0
0.717	0.734	0	3.16	0
0.75	0.7	1.54	2.82	2.956
0.783	0.67	1.392	2.534	2.654
0.841	0.62	1.108	2.09	2.178
0.891	0.582	0.876	1.764	1.83
0.932	0.554	0.732	1.518	1.568
0.935	0.55	0.72	1.498	1.546
0.939	0.548	0.71	1.478	1.524
0.942	0.546	0.7	1.458	1.504
0.946	0.544	0.692	1.438	1.482
0.95	0.542	0.68	1.418	1.456

0.75 are depicted in Fig. 3. The intensity distribution of the RP beam on the optical axis is 0 when NA is low. Hence, the NA is required to meet certain requirements (NA$>$0.75) for the generation of the optical needle induce by RP beams. In contrast, such a phenomenon does not appear in the focusing spot of the APV beam, thus making it possible to generate optical needles with a small NA. In addition, we learn from Table I that the focusing spot of the APV beam is smaller than that of the RP beam. Therefore, the AP beam has significant advantages in the generation of optical needles due to its smaller focusing spot and no strict requirements on focusing structure.

3.2 Influence of NA on Focusing Spot

The FWHM and LFWHM of the APV beams under different NAs are summarized in Table I and shown in Fig. 4. In general, the spot size and DOF of a focusing system are determined to be $K_1\lambda$/NA and $K_2\lambda$/NA^2, respectively, where K_1 and K_2 are proportional coefficients. The FWHM shown in Fig. 4(a) also satisfies the relationship of $K_1\lambda$/NA. Therefore, the relationship between

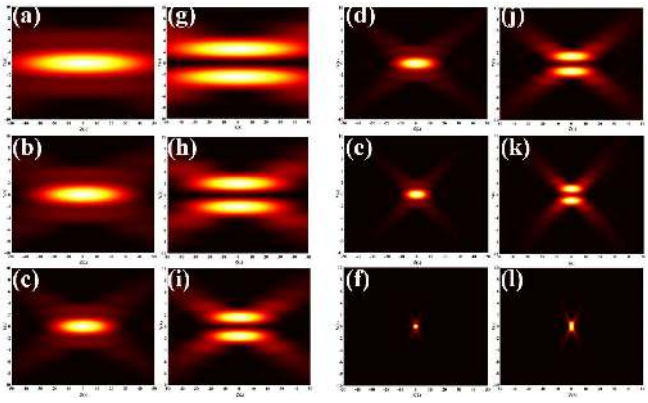

Fig. 3. Intensity distributions along the optical axis. (a–f) APV beam and (g–l) RP beam, when NA = 0.16, 0.198, 0.247, 0.295, 0.389, 0.75, respectively.

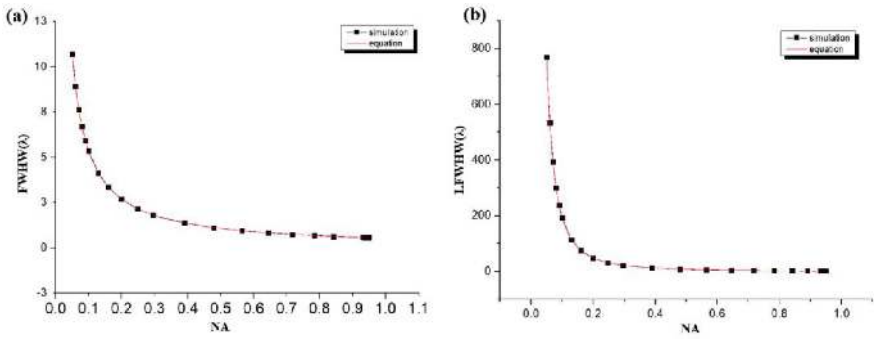

Fig. 4. Variation of FWHM and LFWHM with NA. (a) FWHM. (b) LFWHM.

FWHM and NA can be obtained by analyzing and fitting the data points:

$$FWHM = 0.53421\lambda/NA. \tag{5}$$

The curve fitting based on (5) is also plotted in Fig. 4(a) for comparison. The perfect fitting with the data points indicates that the FWHM of the focusing spot can be correctly calculated according to the equation. In addition, the fact of $K_1 = 0.53421$ further proves the advantages of using the APV beam in generating sub-wavelength spots. The LFWHM of the APV beam is listed in Table I and depicted in Fig. 4(b). Similarly, we obtained the relationship between the focusing spot LFWHM and NA:

$$LFWHM = 1.19817\lambda/NA^2. \tag{6}$$

As illustrated in Fig. 4(b), the perfect fitting to the data points indicates that the LFWHM of the APV beam can be correctly calculated according to the equation. The result of $K_2 = 1.91817$ demonstrates the advantages of using the APV beam in generating focusing spots with ultra-long DOF.

Hence, (5)–(6) provide a reference for the calculation of focusing spots of the APV beam. The ratio $K_2/K_1 = 3.5918$ means that the APV beam has a great potential in the generation of the optical needles with a high depth-to-width ratio.

3.3 Influence of Annular Width on Focusing Spot

The influence of the amplitude modulation element on the focusing spot is discussed in this section. In the model of Fig. 2(a), an annular aperture is added, forming the focusing model as shown in

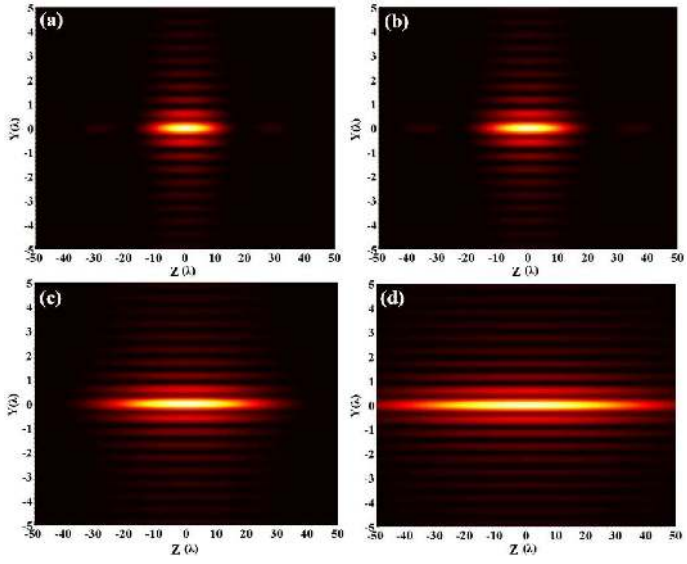

Fig. 5. Light intensity distribution of the focusing spot at different $\theta_{\min}$. (a) $\theta_{\min} = 1.21$. (b) $\theta_{\min} = 1.22$. (c) $\theta_{\min} = 1.23$. (d) $\theta_{\min} = 1.24$.

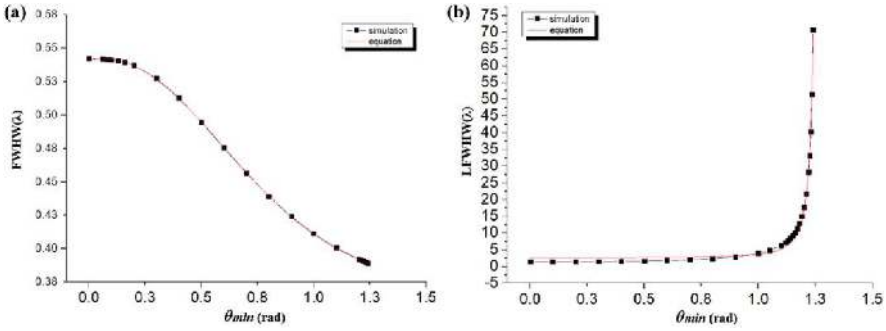

Fig. 6. Variation of (a) FWHM and (b) LFWHM of the focusing spot with $\theta_{\min}$.

Fig. 1, to study the influence of the annular width on the intensity distribution of the focusing spot. The annular width is represented by $\theta_{\max}$ and $\theta_{\min}$. The NA of the objective lens used in the simulation is 0.95, corresponding to $\theta_{\max} = 1.2532$ rad. The variation of the FWHM and LFWHM of the focusing spot at different annular widths are studied by changing $\theta_{\min}$.

Fig. 5 shows the axial intensity distribution of the focusing spot when $\theta_{\min} = 1.21$, 1.22, 1.23, 1.24, which is calculated by Eq. (2). The FWHMs of the focusing spot are 0.3914λ, 0.3908λ, 0.39λ, 0.3894λ, respectively; and the LFWHMs are 21.754λ, 28.252λ, 40.356, 70.804λ, respectively. It is shown in Fig. 6 that the FWHM decreases while the LFWHM increases significantly with the increase of $\theta_{\min}$. In order to analyze the influence of annular width on the focusing spot, the values of FWHM and LFWHM at different $\theta_{\min}$ were obtained and plotted in Fig. 6. The variation trend of FWHM in Fig. 6(a) satisfies the Gaussian distribution, and the relationship between FWHM and $\theta_{\min}$ can be obtained by analyzing the data points, which satisfies the following equation:

$$FWHW = 0.37492 + \left(\frac{0.22315}{1.06449 * \sqrt{\pi/2}}\right) \exp\left(-2\frac{(\theta_{\min} - 0.06519)^2}{1.06449^2}\right). \quad (7)$$

The curve obtained by (7) is plotted as the red line in Fig. 6, showing a good agreement with the data points. It is inferred from the equation that the limit of FWHM by focusing an APV annular beam at NA = 0.95 is about 0.375λ. Similarly, the variation trend of LFWHM in Fig. 6(b) satisfies

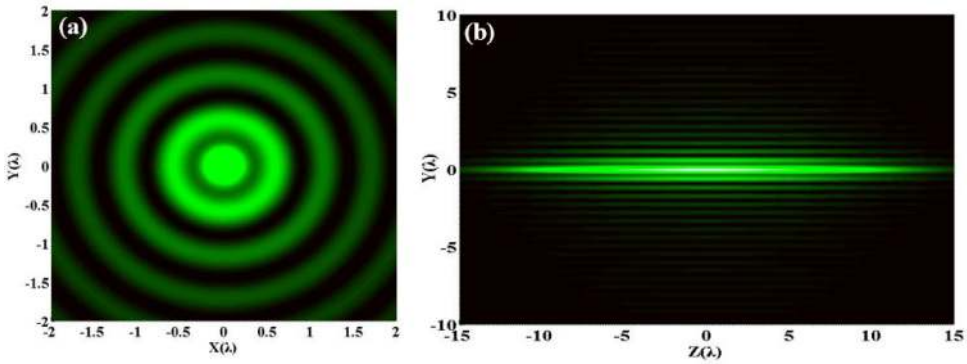

Fig. 7. Simulation results of focusing APV annular beam. (a) Radial intensity distribution. (b) Axial intensity distribution.

the Lorentz distribution, which can be expressed by the following equation:

$$LFWHW = 5.51058 + \frac{0.3118}{\pi\left[4(\theta_{\min} - 1.25936)^2 + \left(2.27457^{-4}\right)^2\right]}. \tag{8}$$

The Lorentz function is used to measure the inequality of income distribution in a country. The curvature of the curve is represented by the Gini coefficient. The larger the Gini coefficient is, the more unequal the income distribution is. Similarly, this function can be used to measure the contribution of incident light from different angles to the DOF. It is considered that the contribution is extremely unequal when the Gini coefficient is higher than 0.4. Here the Gini coefficient of (8) is 0.945, indicating that the large angle components mainly contribute to the DOF. Therefore, the optical needle with the sub-wavelength spot and ultra-long DOF can be generated by focusing the APV annular beam with a high NA objective lens.

Based on the above conclusions, we propose to use the AP beam, a SPP with topological charge of 1, an annular aperture with width of 80 um, and an objective les of NA $= 0.95$ to generate the ultra-long optical needle. The theoretical calculation results of the model are shown in Fig. 7. Fig. 7(a) shows the radial intensity distribution of the focusing spot at the focal point, and the FWHM of the focusing spot is 0.398λ. Fig. 7(b) shows the axial intensity distribution of the focusing spot, and the LFWHM is 17.7λ. Hence, our design generates a focusing spot with a sub-wavelength size and ultra-long DOF.

4. Experimental Results

In this section, the designed model will be experimentally verified. Firstly, the required annular aperture and SPP were fabricated by lithography. Secondly, the experimental system was designed and built to generate the optical needle. Finally, a focusing spot with FWHM of 0.416λ and LFWHM of 15.6λ was obtained, leading to an expected depth-to-width ratio of 37.5:1.

4.1 Fabrication of Annular Aperture and SPP

The designed annular aperture was fabricated by the combination of lithography technology and chemical etching.

The microscope image of the fabricated annular aperture is shown in Fig. 8. Note that the black area corresponds to the transparent region due to the use of a reflection-type microscope. The inner diameter of the annular aperture is measured to be 3901.482 μm with an error of 1.482 μm. The annular width is 80.7 μm with an error of only 0.7 μm. Note that all the above errors are within the acceptable range.

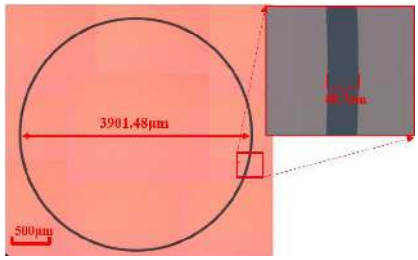

Fig. 8. Structure of the annular aperture.

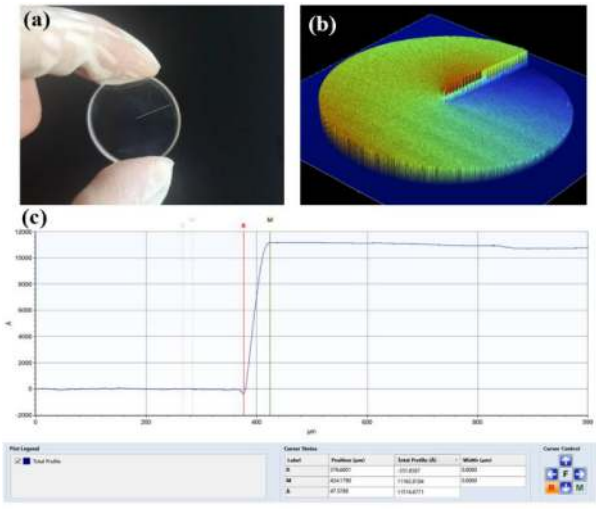

Fig. 9. Structure of SPP. (a) Picture. (b) 3D profiles. (c) Step heights.

The SPP with topological charge of 1 was fabricated by the lithography technology, which has been studied and reported by us in 2015 [36].

The picture of the obtained element is shown in Fig. 9(a). The diameter D is 25.4 mm, the suitable wavelength λ is 532 nm, and the phase modulated range is 2π. In addition, the 3D profiles of the SPPs were tested by an optical surface profiler (Counter GT) and the step heights were tested by a step profiler. The results are shown in Fig. 9(b-c). We can clearly distinguish the finely and sleekly profile of the SPP with a step height of 1.151 μm, showing an excellent agreement with the theoretical depth of 1.154 μm.

4.2 Experimental Setup

Fig. 10 shows the experimental setup. The light source is a He-Ne laser emitting at 532 nm. The size and light intensity of the beam are modulated after passing through an adjustable attenuator (AA) and aperture (A1). The linearly polarized laser beam generated by a polarizer (P1) is converted into an azimuthally polarized Laguerre-Gaussian wave with a polarization converter (PC). PC is similar to a 1/2 wave plate that fast axis continuously rotation, resulting the polarization direction of the linearly polarized light is rotated by different angles after passing through the converter, thereby generating AP beam. After the phase modulation of a spiral phase plate (SPP), the beam passes through an annular aperture (A2) to form an APV annular beam. Finally, an optical needle generated by focusing APV annular beam with an objective lens (L1) of NA $= 0.95$. However, the spot size of the needle is smaller than the pixel size of the CCD camera. Therefore, we use a 100 $\times$ magnification microscope system to obtain the intensity distribution of the optical needle,

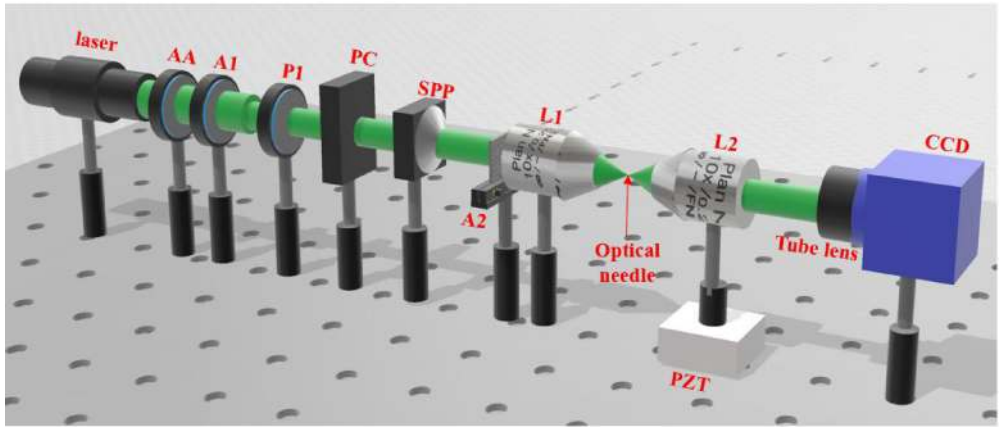

Fig. 10. Experimental setup.

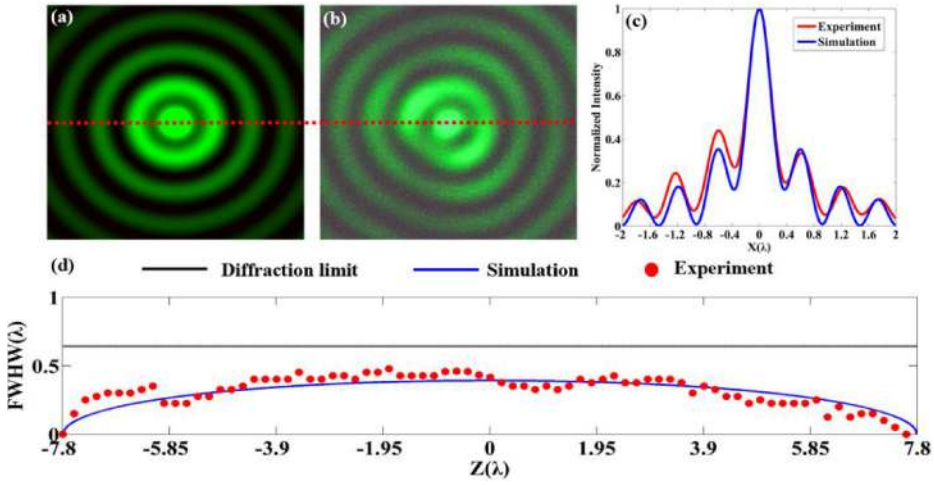

Fig. 11. Radial light intensity. (a) Result of simulation. (b) Result of experiment. (c) Comparison of simulation and experiment. (d) The FWHM along the optical axis.

which consisting of a 100 $\times$ objective lens (L2) with NA $=$ 0.95 and a CCD camera (resolution of 4608 $\times$ 3456 and pixel size 1.335 μm $\times$ 1.335 μm) with a tube lens. The objective lens is mounted on a nano-positioner (PZT) with a linear scanning rang of 200 μm to obtain the information of DOF.

4.3 Results and Discussion

The system in Fig. 10 was used for experimental verification. The radial light intensity distribution at the focal point (2 mm from the entry pupil) was obtained and shown in Fig. 11(b), the simulation result is shown in Fig. 11(a) for comparison. In Fig. 11(c), the experimental results of the light intensity distribution on the x axis are compared with the simulation to show a good agreement. The FWHM of the focusing spot is 0.416λ, compared to the theoretical value 0.398λ. Similarly, the theoretical and experimental values of the FWHM along the optical axis are compared in Fig. 11(d), again showing a good agreement. The discrepancy between the theoretical and experiment results is attributed to the difficulties in the optical alignment, especially for such an ultra-long optical needle. In addition, the FWHM is smaller than the diffraction limit 0.6421λ (0.61λ/NA), thus demonstrating the superiority of the APV annular beam in breaking the diffraction limit.

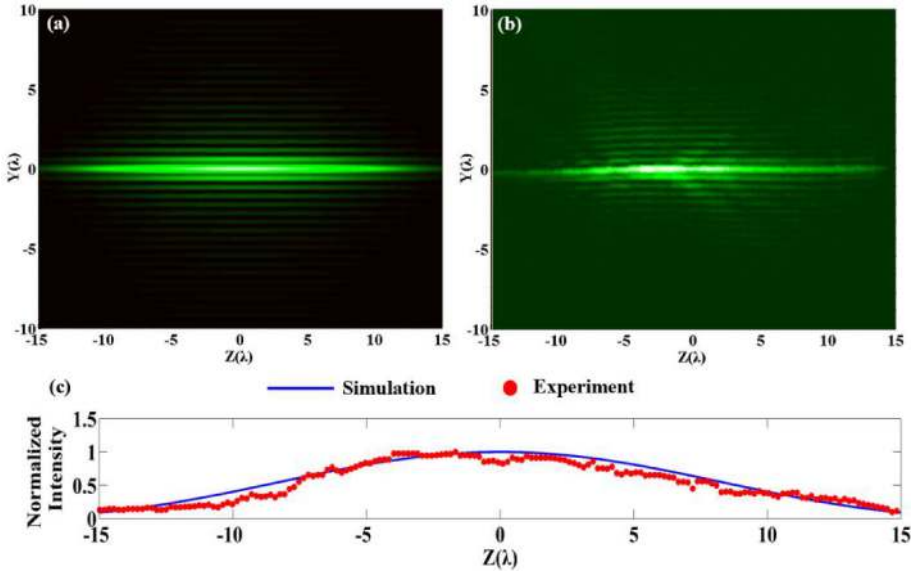

Fig. 12. Axial light intensity. (a) Result of simulation. (b) Result of experiment. (c) The intensity on the optical axis.

In order to verify the DOF of the focusing spot, we used the PZT to conduct the axial scanning to obtain the intensity distribution of the optical needle along the optical axis. The comparison of the experimental and theoretical results is illustrated in Fig. 12.Fig. 12(c) compares the intensity distribution on the optical axis between the experiment and theory. Furthermore, the LFWHM value is measured to be 15.6λ, compared to the theoretical value is 17.7λ. The experimental result is slightly lower than the theory, which is attributed to the influence of laser stability, uniformity of the incident beam, external environmental disturbance, and target surface quality of the CCD. Finally, the FWHM and LFWHM of the focusing spot is measured to be 0.416λ and 15.6λ, respectively, leading to a depth-width-ratio 37.5:1, proving the feasibility of generating an ultra-long optical needle induced by AP beam.

5. Conclusion

A method of generating an ultra-long optical needle by focusing an AP beam is proposed and verified by experiment. We demonstrated the superiority of using the AP beam in generating such an ultra-long optical needle. The variation of the intensity distribution of the focusing spot under different numerical apertures and ring widths was studied, and the corresponding functional relation is given. The results show that the optical needle with a subwavelength spot and ultra-long DOF can be generated by using the APV annular beam focused by a high NA lens. Finally, an annular aperture and a SPP were designed and fabricated for experimental verification. The focusing spot obtained by experiment has a FWHM of 0.416λ and a LFWHM of 15.6λ. The ultra-long optical needle is expected to be widely applied in lithography, optical data storage and super-resolution imaging.

References

[1] Z. Gan *et al.*, "Three-dimensional deep sub-diffraction optical beam lithography with 9 nm feature size," *Nat. Commun.*, vol. 4, no. 2061, pp. 1–7, Jun. 2013.
[2] Y. Zhang and J. Bai, "Improving the recording ability of a near-field optical storage system by higher-order radially polarized beams," *Opt. Exp.*, vol. 17, no. 5, pp. 3698–3706, Feb. 2009.

[3] D. Lu and Z. Liu, "Hyperlenses and metalenses for far-field super-resolution imaging," *Nat. Commun.*, vol. 3, no. 1205, pp. 1–9, Nov. 2012.
[4] R. Daniel *et al.*, "Enhanced resolution beyond the abbe diffraction limit with wavelength-scale solid immersion lenses," *Opt. Lett.*, vol. 35, no. 12, pp. 2007–2009, Jun. 2010.
[5] L. G. Pamela and G. H. Dennis, "Diffraction characteristics of the azimuthal Bessel–Gauss beam," *J. Opt. Soc. Amer. A.*, vol. 13, no. 5, pp. 962–966, May 1996.
[6] S. Quabis, R. Dorn, and M. Eberler, "Focusing light to a tighter spot," *Opt. Commun.*, vol. 179, no. 1-6, pp. 1–7, May 2000.
[7] R. H. Jordan and D. G. Hall, "Free-space azimuthal paraxial wave equation: The azimuthal Bessel–Gauss beam solution," *Opt. Lett.*, vol. 19, no. 7, pp. 427–429, Apr. 1994.
[8] S. Zhou *et al.*, "Creation of radially polarized optical fields with multiple controllable parameters using a vectorial optical field generator," *Photon. Res.*, vol. 4, no. 5, pp. 35–39, Oct. 2016.
[9] X. Wang *et al.*, "Enhancing plasmonic trapping with a perfect radially polarized beam," *Photon. Res.*, vol. 6, no. 9, pp. 847–852, Sep. 2018.
[10] Y. Zhou *et al.*, "Self-starting passively mode-locked all fiber laser based on carbon nanotubes with radially polarized emission," *Photon. Res.*, vol. 4, no. 6, pp. 327–330, Dec. 2016.
[11] K. Youngworth and T. Brow, "Focusing of high numerical aperture cylindrical-vector beams," *Opt. Exp.*, vol. 7, no. 2, pp. 77–87, Jun. 2000.
[12] H. Wang *et al.*, "Creation of a needle of longitudinally polarized light in vacuum using binary optics," *Nat. Photon.*, vol. 2, no. 8, pp. 501–505, Jun. 2008.
[13] K. Huang *et al.*, "Design of DOE for generating a needle of a strong longitudinally polarized field," *Opt. Lett.*, vol. 35, no. 7, pp. 965–967, Apr. 2010.
[14] H. Guo *et al.*, "Tight focusing of a higher-order radially polarized beam transmitting through multi-zone binary phase pupil filters," *Opt. Exp.*, vol. 21, no. 5, pp. 5363–5372, Aug. 2013.
[15] J. Lin *et al.*, "Achievement of longitudinally polarized focusing with long focal depth by amplitude modulation," *Opt. Lett.*, vol. 36, no. 7, pp. 1185–1187, Apr. 2011.
[16] J. Chen *et al.*, "Tight focus of a radially polarized and amplitude-modulated annular multi-Gaussian beam," *Chin. Phys. B.*, vol. 20, no. 11, pp. 291–295, Jun. 2011.
[17] M. G. Banaee and M. Selim, "Sub-λ/10 spot size in semiconductor solid immersion lens microscopy," *Opt. Commun.*, vol. 315, pp. 108–111, Nov. 2014.
[18] Y. Zhan *et al.*, "Creation of an ultra-long depth of focus super-resolution longitudinally polarized beam with a ternary optical element," *J. Opt.*, vol. 15, no. 7, pp. 536–544, May 2011.
[19] A. Yu *et al.*, "Creation of sub-diffraction longitudinally polarized spot by focusing radially polarized light with binary phase lens," *Scientific Reports*, vol. 6, no. 38859, pp. 1–9, Dec. 2016.
[20] R. Martínez-Herrero and D. Maluenda, "Synthesis of light needles with tunable length and nearly constant irradiance," *Scientific Reports*, vol. 8, no. 2657, pp. 1–10, Feb. 2018.
[21] G. Yuan and T. R. Rogers, "Planar super-oscillatory lens for sub-diffraction optical needles at violet wavelengths," *Scientific Reports*, vol. 4, no. 6333, pp. 1–7, Sep. 2014.
[22] H. Li *et al.*, "Theoretical generation of arbitrarily homogeneously 3D spin-orientated optical needles and chains," *Opt. Exp.*, vol. 27, no. 5, pp. 6047–6056, Feb. 2019.
[23] S. Wang *et al.*, "Ultralong pure longitudinal magnetization needle induced by annular vortex binary optics," *Opt. Lett.*, vol. 39, no. 17, pp. 5022–5025, Mar. 2014.
[24] H. Li *et al.*, "Ultra-long magnetization needle induced by focusing azimuthally polarized beams with a spherical mirror," *Appl. Opt.*, vol. 57, no. 9, pp. 2069–2072, Mar. 2018.
[25] F. Qin, K. Huang, and J. Wu, "Shaping a subwavelength needle with ultra-long focal length by focusing azimuthally polarized light," *Scientific Reports*, vol. 5, no. 9977, pp. 1–9, May 2015.
[26] X. Hao *et al.*, "Phase encoding for sharper focus of the azimuthally polarized beam," *Opt. Lett.*, vol. 35, no. 23, pp. 3928–3930, Dec. 2010.
[27] G. H. Yuan, S. B. Wei, and X.-C. Yuan, "Nondiffracting transversally polarized beam," *Opt. Lett.*, vol. 36, no. 17, pp. 3479–3481, Jun. 2014.
[28] S. Zhang *et al.*, "Synthesis of sub-diffraction quasi-non-diffracting beams by angular spectrum compression," *Opt. Exp.*, vol. 25, no. 22, pp. 127104–127118, Oct. 2017.
[29] G. Chen *et al.*, "Planar binary-phase lens for super-oscillatory optical hollow needles," *Scientific Reports*, vol. 7, no. 4697, pp. 1–10, Jul. 2017.
[30] K. Lalithambigai and P. M. Anbarasan, "Creation of super-length optical tube by phase modulated azimuthally polarized beam with multi-zone phase filter," *Optik*, vol. 126, no. 5, pp. 554–557, Feb. 2015.
[31] Y. Liu *et al.*, "The use of azimuthally polarized sinh-Gauss beam in STED microscopy," *J. Opt.*, vol. 17, no. 4, pp. 1–8, Mar. 2015.
[32] G. Rui *et al.*, "Manipulation metallic nanoparticle at resonant wavelength using engineered azimuthally polarized optical field," *Opt. Exp.*, vol. 24, no. 7, pp. 7212–7223, Apr. 2016.
[33] Y. Xue *et al.*, "Sharper fluorescent super-resolution spot generated by azimuthally polarized beam in STED microscopy," *Opt. Exp.*, vol. 20, no. 16, pp. 17653–17666, Jul. 2012.
[34] B. Richards and E. Wolf, "Electromagnetic diffraction in optical systems. I. An integral representation of the image field," *Proc. R. Soc. Lond.*, vol. 253, no. 1274, pp. 349–357, Oct. 1959.
[35] B. Richards and E. Wolf, "Electromagnetic diffraction in optical systems, II. Structure of the image field in an aplanatic system," *Proc. R. Soc. Lond.*, vol. 253, no. 1274, pp. 358–379, Oct. 1959.
[36] L. Shi *et al.*, "One exposure processing to fabricate spiral phase plate with continuous surface," *Opt. Exp.*, vol. 23, no. 7, pp. 8620–8629, Apr. 2016.